

3D in Natural Random Refractive Distortions

Marina Alterman^a and Yoav Y. Schechner^b

^aNorthwestern University, Evanston, USA

^bTechnion - Israel Institute of Technology, Haifa, Israel

ABSTRACT

Random distortions naturally affect images taken through atmospheric turbulence or wavy water. They pose new 3D recovery problems. Distortions are caused by the volumetric field of turbulent air or the 3D shape of water waves. We show methods that recover these 3D distorting media. Moreover, it is possible to triangulate objects beyond the refracting medium. Applications include sensing and study of random refractive media in nature, and enhanced imaging including possibilities for a virtual periscope.

Keywords: Refraction, Triangulation, Turbulence, Stereo, Tomography, Computational Photography, Computer Vision

1. INTRODUCTION

Consider a camera that is imaging an object. Changes of the refractive index of a medium along a line of sight (LOS) cause distortion¹⁻³ in acquired images (Fig. 1). Such changes are created by atmospheric turbulence (See Fig. 2). Hence, images that are acquired in the presence of atmospheric turbulence suffer from geometric distortions. The refractive index of a medium changes along a LOS also when looking through a water-air interface (WAI). The distortions are particularly strong when a submerged viewer (e.g. a diver) looks obliquely upwards from beneath a wavy water surface (see Fig. 3). We study various 3D vision challenges in random refractive media.

First, we begin (Sec. 2) with a stochastic multiview approach in atmospheric turbulence. Random refractive distortions due to turbulence offer information about the medium itself.⁴ We *exploit* random image distortions as a means to estimate the 3D (volumetric) distribution of *turbulence strength* (TS). The strength of turbulence is a statistical measure of local variations in the medium.^{5,6} Meteorologists rely on turbulence strength to understand formation of clouds and efficiency of wind turbines.⁷ Moreover, determining which areas have stronger or weaker turbulence can optimize free-space optical relay of communication and power.⁷

The variances in image projections of background features are computed by tracking those features over a few hundred frames. The projection variance at each pixel at each camera viewpoint is simply a weighted integral of the turbulence strength along the respective pixels' LOS. The LOSs of all pixels from *multiple* viewpoints crisscross the turbulence field. Estimating the TS's volumetric distribution is then equivalent to solving a linear tomography problem. While linear tomography is common in medical imaging, the specific structure here is different. Thus, our domain and model form a new addition to the set of tomographic problems, which have recently stimulated interest in computational photography and vision.⁸⁻¹⁷

Sec. 3 treats oblique views upwards through a wavy WAI. This is highly challenging, since the distortions in this scenario are much stronger than in atmospheric turbulence. Moreover, this setup is related to biological vision: it is experienced by submerged animals seeking to detect prey or avoid predators, which are airborne or on land. Oblique upward vision through a WAI can function as a virtual periscope for submariners and divers, who wish to avoid using attention-drawing physical periscopes. Sec. 3 takes a stochastic multiview approach to this task. Multiview images acquired simultaneously in a wide stereo baseline have uncorrelated distortions. Measurements of an object's random projection from multiple views and times lead to a likelihood function of

Further author information: (Send correspondence to M.A.)

M.A.: E-mail: amarinago@gmail.com

Y.Y.S.: E-mail: yoav@ee.technion.ac.il

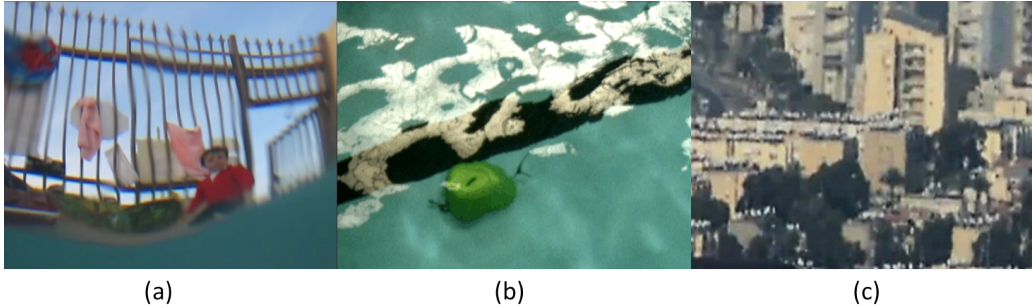


Figure 1. (a) A frame of an airborne scene, taken by a submerged camera. (b) A sample frame of an underwater scene, taken by a downward looking camera through the water surface. (c) Sample image taken through a turbulent atmosphere.

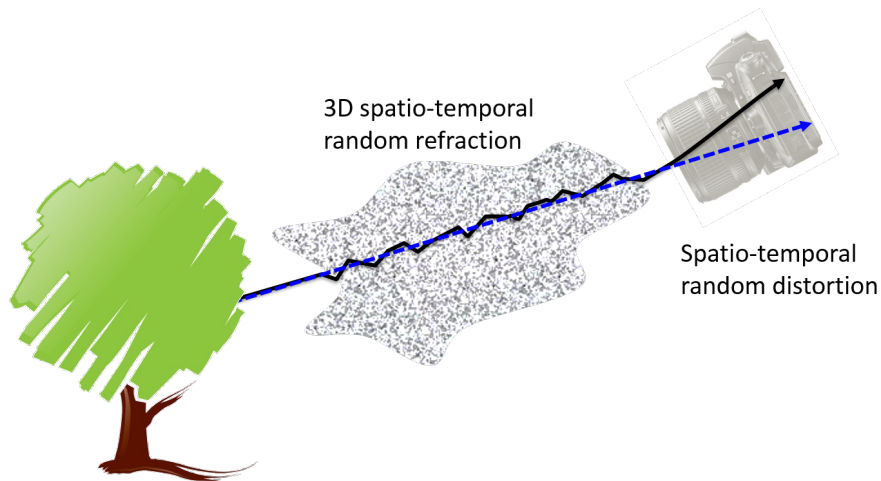


Figure 2. The dashed line represents imaging through a non-turbulent medium while the solid line illustrates distortion caused by a turbulence in 3D.

the object's 3D location. Maximum likelihood (ML) estimates the 3D location, while the effective support of the likelihood function informs of the location uncertainty. Sec. 4 presents a deterministic multiview approach to water distorted image correction. By estimating the 3D WAI shape, distortions attributed to the waves can be countered. We develop this idea, demonstrate it by performing lab and field experiments, and analyze its limitations.

2. PASSIVE TOMOGRAPHY OF TURBULENCE STRENGTH

There is an LOS between a background object point and a camera at distance L away. Without turbulence, the LOS has an angle of arrival (AOA) relative to the optical axis. Fluctuations of the atmospheric refractive index lead to random refractions of propagating light (see Fig. 2). Hence turbulence perturbs the LOS. Due to turbulence, random image distortions are observed over time. Each temporal frame is spatially distorted. We give here the essence in brief, while the proofs and full details can be found in our article.¹⁸ For a wide-angle radiating source (a point source), models established in the literature^{4,19} express the variance σ_{AOA}^2 of the AOA by integration along the LOS. Let f be the focal length of the camera. Then, the image pixel displacement has

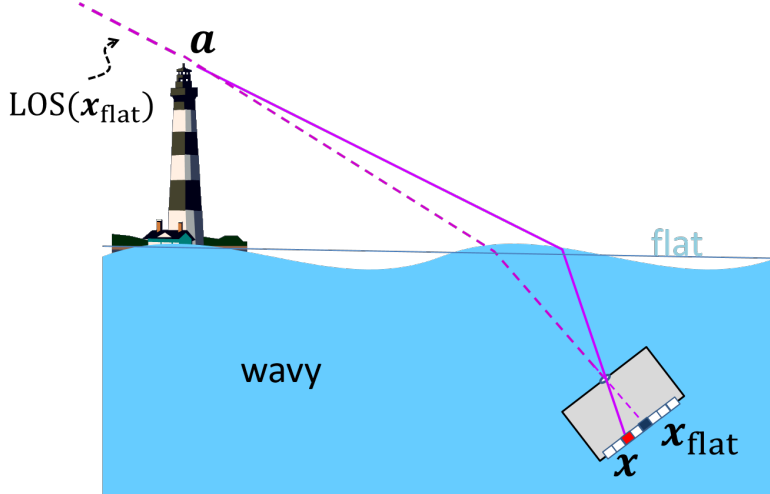


Figure 3. Imaging through a water-air-interface. The camera is submerged and stares obliquely upward at an object in the air. The dashed line represents imaging through a flat water surface (blue pixel), while the solid line represents distortion caused by wavy water (red pixel).

variance

$$\sigma_{\mathbf{x}}^2 \approx f^2 \left[\frac{d \tan(\text{AOA})}{d \text{AOA}} \right]^2 \sigma_{\text{AOA}}^2 = f^2 \frac{1}{\cos^4(\text{AOA})} \sigma_{\text{AOA}}^2,$$

$$\sigma_{\text{AOA}}^2 = 2.914 D^{-1/3} \int_0^L C_n^2[\mathbf{X}(s)] \left(\frac{s}{L} \right)^{5/3} ds, \quad \mathbf{X} \in \text{LOS}. \quad (1)$$

Here $\mathbf{X} = (X, Y, Z)$ is the spatial location, D is the camera aperture diameter, $s = 0$ corresponds to the background object location, while $s = L$ corresponds to the lens pupil location. The parameter C_n^2 is the refractive index structure constant^{4,19} which expresses TS. High values of C_n^2 imply strong turbulence, while $C_n^2 = 0$ means that the air is not turbulent. The TS changes spatially, thus we denote it $C_n^2(\mathbf{X})$. High variance in the map means that a LOS passes through more turbulence, than at pixels exhibiting low displacement variance.

We discretize the volume domain into a 3D grid of voxels and approximate C_n^2 as constant in each voxel. Define a $N_{\text{pixels}} \times N_{\text{voxels}}$ matrix \mathbf{A} , whose elements represent intersections of all LOSs and all voxels. Matrix \mathbf{A} is sparse. Column-stack the measured AOA variances $\sigma_{\mathbf{x}}^2$ to vector \mathbf{m} . Column-stack the unknown C_n^2 for all voxels to vector \mathbf{c} . Then, Eq. (1) can be posed in vector form as¹⁸ $\mathbf{m} = \mathbf{A}\mathbf{c}$. This linear system of equations can be solved by any standard solver. For example, it may be possible to use constrained and/or regularized least-squares:

$$\hat{\mathbf{c}} = \arg \min_{\mathbf{c}} (\|\mathbf{m} - \mathbf{A}\mathbf{c}\|^2 + \lambda \|\nabla^2 \mathbf{c}\|^2) \quad \text{s.t. } \mathbf{c} \geq \mathbf{0}, \quad (2)$$

where λ weights a spatial smoothness regularizing term. When \mathbf{A} is large, we use the Simultaneous Algebraic Reconstruction Technique (SART)²⁰ as the solver.

We made an outdoor experiment on a sunny day, from 11:00AM until 2:30PM. Around noon, atmospheric turbulence should be the strongest and stationary over several hours.²¹ The scene is Haifa Bay area. It is a valley with major industrial facilities interleaved by agricultural areas and some towns. We used a Nikon D7100 DSLR camera with a telephoto lens of $f = 300\text{mm}$, $F\# = 14$ and exposure time of $1/600\text{sec}$. To gain a wide field of view (FOV), multiple narrow FOV videos were collected. We shot 30fps HD videos of ≈ 100 temporal frames for each narrow FOV. The scene was imaged from six viewpoints on the surrounding hills. Sample images of views and a stitched panorama are shown in Fig. 4. The data is available on-line.²²

We used Google maps to locate the coordinates of multiple known landmarks in the valley landscape. We located, overall, 360 landmarks across all views (Fig. 5[Left]). Then, pixel displacement statistics (mean and

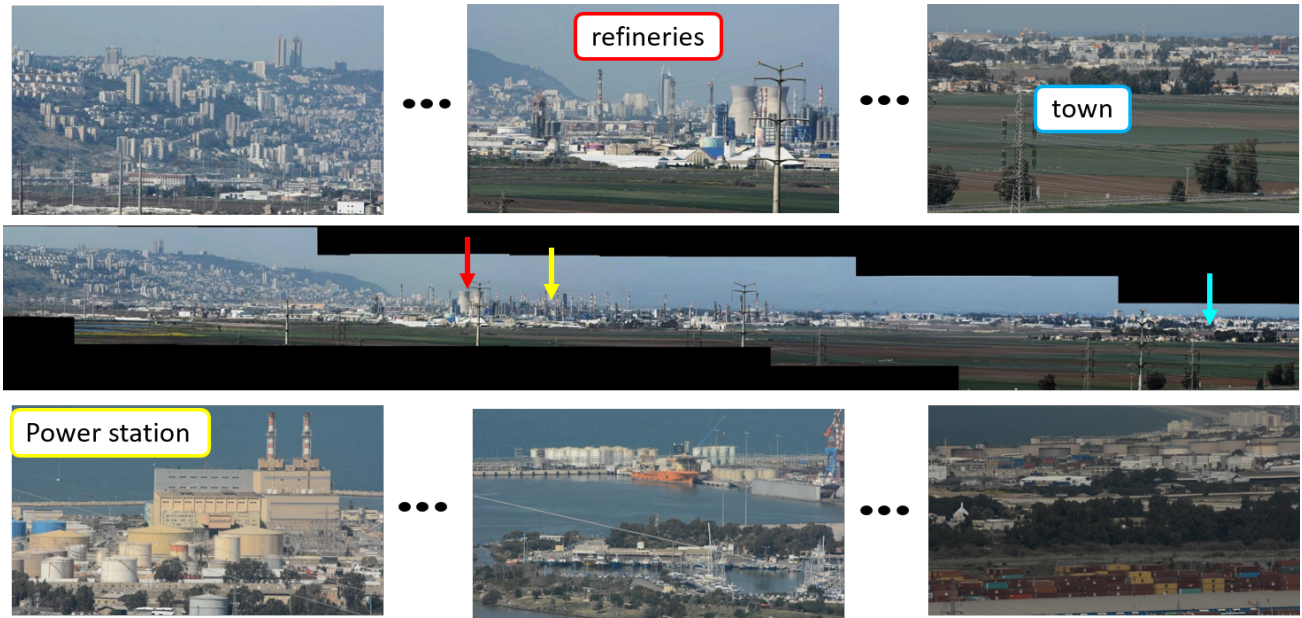


Figure 4. Sample images from an outdoor experiment. Images of different views are shown. Places of interest are indicated on the images and also on the panorama. [Middle] The panorama image of view-2 was created using Microsoft image composite editor. This figure was published by the authors in Proc. ECCV 2014

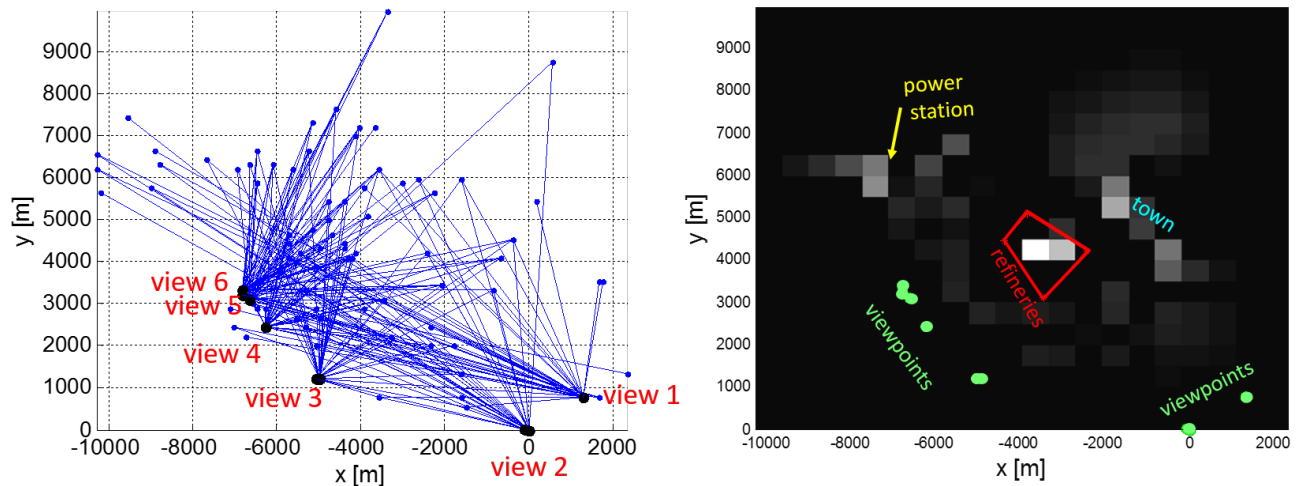


Figure 5. [Left] Experimental setup of the outdoor experiment. Any blue line represents a ray between a viewpoint and an object point. Figure axes are aligned to the compass cardinal directions in our region. [Right] The estimated TS parameter C_n^2 shown in a 2D map. Bright areas represent high values while dark areas represent low values. Regional places of interest are overlaid on the map. Notice the hottest spot is at the oil refineries. This figure was published by the authors in Proc. ECCV 2014

variance) were computed for these landmarks in each temporal sequence of frames to construct the vector \mathbf{m} . The reconstruction area was divided into $20 \times 20 \times 1$ voxels. We used the Laplacian regularization with $\lambda = 0.4$. The estimated turbulence strength parameter (C_n^2) is shown in Fig. 5[Right] as a 2D map. The positions of the cameras are overlaid in green. A region with strong turbulence was estimated as the refineries plant ($C_n^2 = 1.7 \cdot 10^{-14} m^{-2/3}$). The second-strongest hot-spot was near the power station ($C_n^2 = 0.45 \cdot 10^{-14} m^{-2/3}$).

3. TRIANGULATION IN RANDOM REFRACTIVE DISTORTIONS

We now focus on random refraction in multiview geometry.²³ Consider a submerged stereo system having a baseline b . Viewing an airborne scene from a submerged camera creates a *virtual periscope*. Variables associated with the left or right camera are denoted with L or R, respectively. Each camera views the object through a different WAI portion. The projected image point on the left is distorted (displaced) by \mathbf{d}^L , while the corresponding point on the right image is displaced by \mathbf{d}^R .

The full derivation and the experimental details can be found in our dedicated publication.²⁴ Consider Fig. 3. Under a flat WAI, the object in \mathbf{a} projects to pixel $\mathbf{x}_{\text{flat}}^L$ in camera L. Through a flat WAI, there is one-to-one correspondence between $\mathbf{x}_{\text{flat}}^L$ and a specific LOS, denoted $\text{LOS}(\mathbf{x}_{\text{flat}}^L)$, by back-projection. Hence, any probability density associated with $\mathbf{x}_{\text{flat}}^L$ is also associated with $\text{LOS}(\mathbf{x}_{\text{flat}}^L)$. Under a flat WAI, the object in \mathbf{a} projects to pixel $\mathbf{x}_{\text{flat}}^R$ in camera R. Since the WAI is wavy, \mathbf{a} projects to pixel $\mathbf{x}^R(t)$, at time t , while $\mathbf{x}_{\text{flat}}^R$ is unknown. In this work we assume that between the views, correspondence of image points is established. In other words, we know that the measurement pixel set $\{\mathbf{x}^L(t), \mathbf{x}^R(t)\}_t$ corresponds to the same 3D object point, but we do not know where the object is.

The probability density function (PDF) of imaging \mathbf{a} at \mathbf{x}^L is²⁴

$$p(\mathbf{x}^L | \mathbf{x}_{\text{flat}}^L) \approx G \exp \left[-\frac{1}{2} (\mathbf{x}^L - \mathbf{x}_{\text{flat}}^L)^T \boldsymbol{\Sigma}_{\mathbf{x}}^{-1} (\mathbf{x}^L - \mathbf{x}_{\text{flat}}^L) \right] \sim p(\mathbf{x}_{\text{flat}}^L | \mathbf{x}^L), \quad (3)$$

where G is a normalization factor and $\boldsymbol{\Sigma}_{\mathbf{x}}$ is the 2×2 covariance matrix which depends on the WAI roughness, the camera parameters²⁴ and somewhat on \mathbf{x}_{flat} . Eq. (3) sets a probability density $p[\mathbf{x}_{\text{flat}}^L | \mathbf{x}^L(t)]$ to each pixel $\mathbf{x}_{\text{flat}}^L$ in the L image plane. Thus, Eq. (3) sets a probability density

$$p[\text{LOS}(\mathbf{x}_{\text{flat}}^L) | \mathbf{x}^L(t)] \sim p[\mathbf{x}^L(t) | \mathbf{x}_{\text{flat}}^L]. \quad (4)$$

So $\forall \mathbf{x}_{\text{flat}}^L$, Eq. (4) back-projects an image-domain PDF to a PDF of all LOSs that can backproject from camera L through a flat WAI.

An LOS is an infinite set of 3D points \mathbf{X} that project to the same image point. A priori, each of these 3D points is equally likely to be the sought object \mathbf{a} . Hence, with any point $\mathbf{X} \in \text{LOS}(\mathbf{x}_{\text{flat}}^L)$, we associate a *likelihood* equivalent to the probability density defined in Eq. (4):

$$l_t^L(\mathbf{X}) \equiv p[\text{LOS}(\mathbf{x}_{\text{flat}}^L) | \mathbf{x}^L(t)] \quad | \quad \mathbf{X} \in \text{LOS}(\mathbf{x}_{\text{flat}}^L). \quad (5)$$

Based on Eqs. (4,5)

$$l_t^L(\mathbf{X}) \sim p[\mathbf{x}^L(t) | \mathbf{x}_{\text{flat}}^L] \quad | \quad \mathbf{X} \in \text{LOS}(\mathbf{x}_{\text{flat}}^L). \quad (6)$$

Similarly to the process involving Eq. (6), we derive an interpolated likelihood $l_t^R(\mathbf{X})$, $\forall \mathbf{X}$, based on

$$l_t^R(\mathbf{X}) \sim p[\mathbf{x}^R(t) | \mathbf{x}_{\text{flat}}^R] \quad | \quad \mathbf{X} \in \text{LOS}(\mathbf{x}_{\text{flat}}^R). \quad (7)$$

We prefer distortions in the multiple views that are mutually *uncorrelated*. Low statistical dependency between multiview measurements means that any new view adds *more information* about the object location. This is achieved if b is significantly larger than the typical WAI-slope correlation length. Then, likelihoods stemming from different frames and viewpoints multiply each other. Overall, for N_{frames} frames, the likelihood is

$$L(\mathbf{X}) = \prod_{t=1}^{N_{\text{frames}}} l_t^L(\mathbf{X}) l_t^R(\mathbf{X}), \quad (8)$$

as illustrated in Fig. 6.

The effective 3D spatial support (orange region in Fig. 6) of $L(\mathbf{X})$ represents the 3D domain in which the airborne object point is likely to reside. The more viewpoints and temporal frames, the narrower this domain becomes. ML yields an estimate of an optimal airborne 3D object location.

$$\hat{\mathbf{a}} = \underset{\mathbf{X}}{\text{argmax}} L(\mathbf{X}). \quad (9)$$

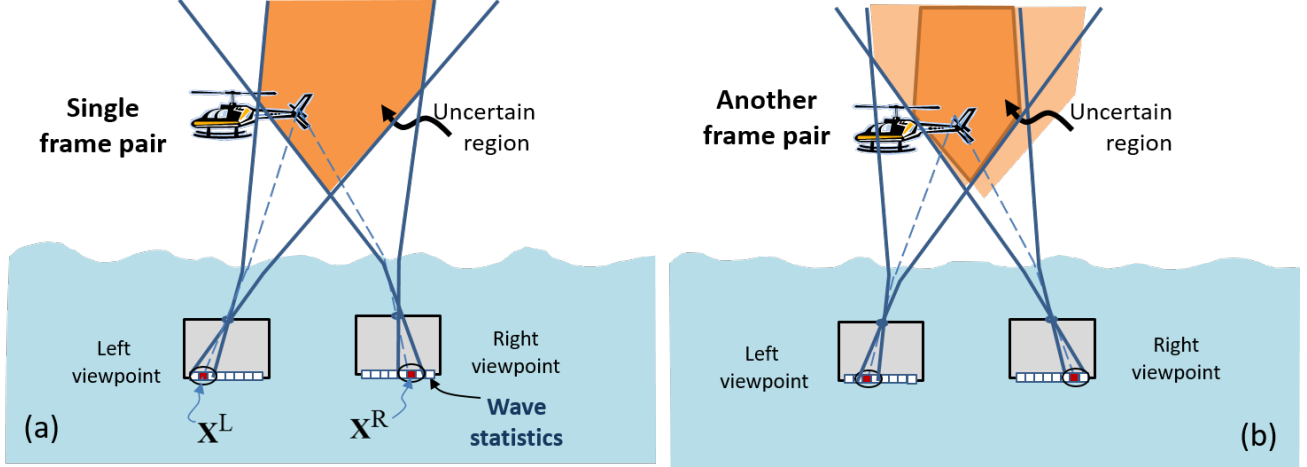


Figure 6. Airborne position likelihood. (a) By projecting the uncertainties around \mathbf{x}^L and \mathbf{x}^R , the effective 3D spatial support (orange region) of the overlap represents the 3D domain in which the airborne object point is likely to reside. (b) Additional temporal frames narrow this domain. © 2013 IEEE. Reprinted, with permission, from *Triangulation in Random Refractive Distortions* by Alterman et al, Proc. ICCP.

We performed an experiment at an indoor swimming pool. We used a pair of Canon HV-30 camcorders, each in an underwater housing. Their baseline was $b = 27.5$ cm. Refer to²⁴ for more experiments and further technical details. The upward camera stereo pair was mounted on a tripod and submerged. An object (potato head doll) was placed 1.6m above the rig. The 3D position estimated by our method evolved over time t , as N_{frames} in Eq. (8) increased from 1 to 19. Also the uncertainty of the estimation evolved (gradually reducing). This is illustrated in Fig. 7: the color coding of the ellipsoids indicate temporal evolution of the estimation: blue to red. The estimated height is $\hat{Z} = 1.6 \pm 0.2$ m, consistent with the ground truth. Each new frame introduces additional information. Thus, the support of the 3D likelihood function shrinks with time.

4. STELLA MARIS: STELLAR MARINE REFRACTIVE IMAGING SENSOR

Telescopes view celestial scenes through a random refracting medium: the turbulent atmosphere (Fig. 8a). Astronomical image degradation can be largely countered by adaptive optics and computational steps, based on an estimate of the refractive disturbance. This estimate is obtained by measuring a known *guide star* using, typically, a Shack-Hartmann wavefront sensor. In analogy, images taken by a submerged virtual periscope are degraded by the random refractive WAI, and estimation of this refractive disturbance would facilitate compensation (Fig. 8b). The analogy of the problem points to our solution: the WAI can be estimated by measuring a known guide star through the WAI, simultaneously with viewing the scene of interest. Our stellar guide is obvious: the *Sun*. It is observed over an array of submerged locations, in analogy to a Shack-Hartmann astronomical sensor.²⁵

Consider Fig. 9. Component \mathcal{V} of the imaging sensor is the viewing camera. It views the airborne scene through the wavy WAI. Component \mathcal{S} is the stellar-guided wave slope-sensor, which we now briefly describe. Full details of this method are given in our full-length paper.²⁶

The WAI-slope sensor includes a horizontal array of pinholes. A sunray refracts by the WAI, then passes through a pinhole at 3D location \mathbf{h} , and irradiates a spot on the diffuser (Fig 9), at 3D location \mathbf{p} . The unit vector $\hat{\mathbf{s}}^w$ is the direction of a back-projected sunray in the water, from \mathbf{p} via \mathbf{h} ,

$$\mathbf{s}^w = \mathbf{h} - \mathbf{p} ; \quad \hat{\mathbf{s}}^w = \mathbf{s}^w / \|\mathbf{s}^w\|_2. \quad (10)$$

In air, the unit vector pointing to the Sun is $\hat{\mathbf{s}}^a$. Using a different vector form of Snell's law²⁷ at the water interface,

$$\hat{\mathbf{s}}^a \times \hat{\mathbf{N}} = n\hat{\mathbf{s}}^w \times \hat{\mathbf{N}}. \quad (11)$$

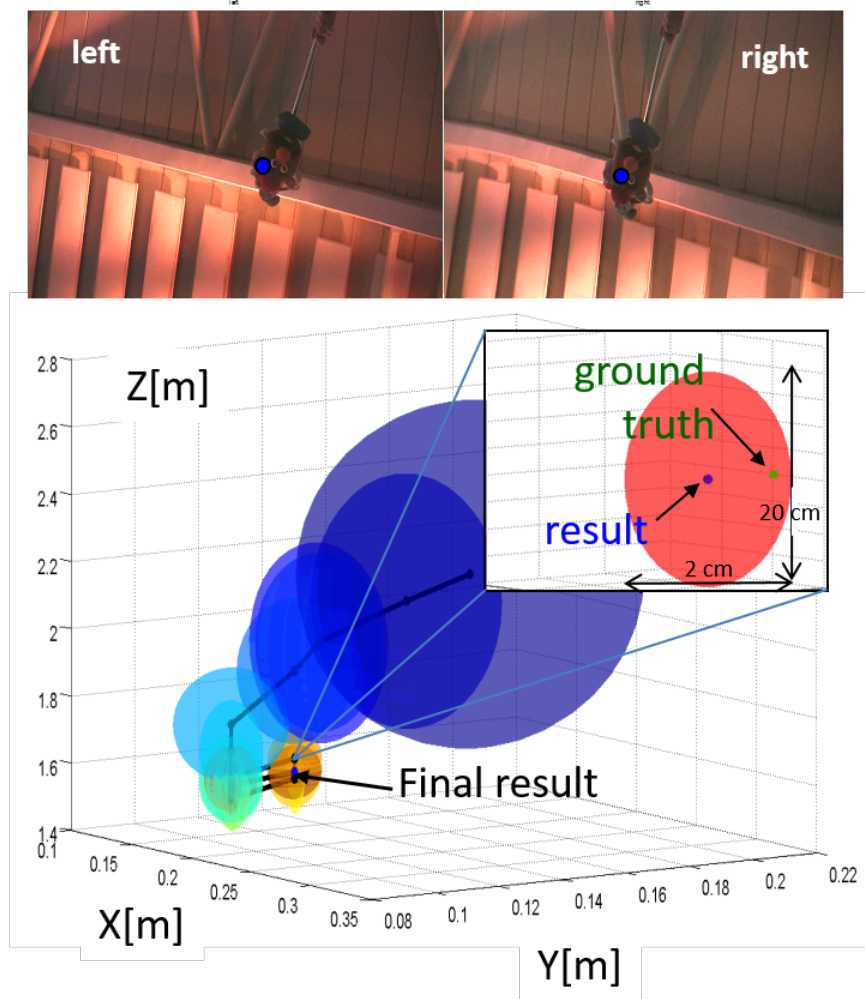


Figure 7. Results of a pool experiment, triangulating a potato head. The illustration shows the estimation evolving as t and N_{frames} increase. Ellipsoids represent the uncertainty of the result, equivalent to the location STD. Time is color coded: blue to red. A zoom-in shows the final result and the ground truth. © 2013 IEEE. Reprinted, with permission, from *Triangulation in Random Refractive Distortions* by Alterman et al, Proc. ICCP.

Here \times is the cross product. In the global coordinate system, the horizontal (x, y) coordinates correspond to the pinhole array axes, and z denotes height above the diffuser plane. The pinhole array is at distance z_h above the diffuser. Using the axial components of the vectors $\hat{\mathbf{s}}^a, \hat{\mathbf{s}}^w$ and $\hat{\mathbf{N}}$, Eq. (11) can be phrased in matrix form,

$$\mathbf{B}\hat{\mathbf{N}} = 0, \quad (12)$$

where

$$\mathbf{B} = \begin{pmatrix} 0 & -s_z^a + ns_z^w & s_y^a - ns_y^w \\ s_z^a - ns_z^w & 0 & -s_x^a + ns_x^w \\ -s_y^a + ns_y^w & s_x^a - ns_x^w & 0 \end{pmatrix}. \quad (13)$$

The vector pointing to the Sun in air, $\hat{\mathbf{s}}^a$, is always known, given the time of image acquisition, geographic location, and compass azimuth of the global coordinate system. Moreover, the vector $\hat{\mathbf{s}}^w$ is extracted from the image data (10). Hence, the matrix \mathbf{B} is known. The WAI normal $\hat{\mathbf{N}}$ is estimated by solving Eq. (12): it is the null subspace of \mathbf{B} . This process is repeated for each pinhole, indexed k , and located at \mathbf{h}_k . It yields a set of sampled vectors $\{\hat{\mathbf{N}}_k\}$.

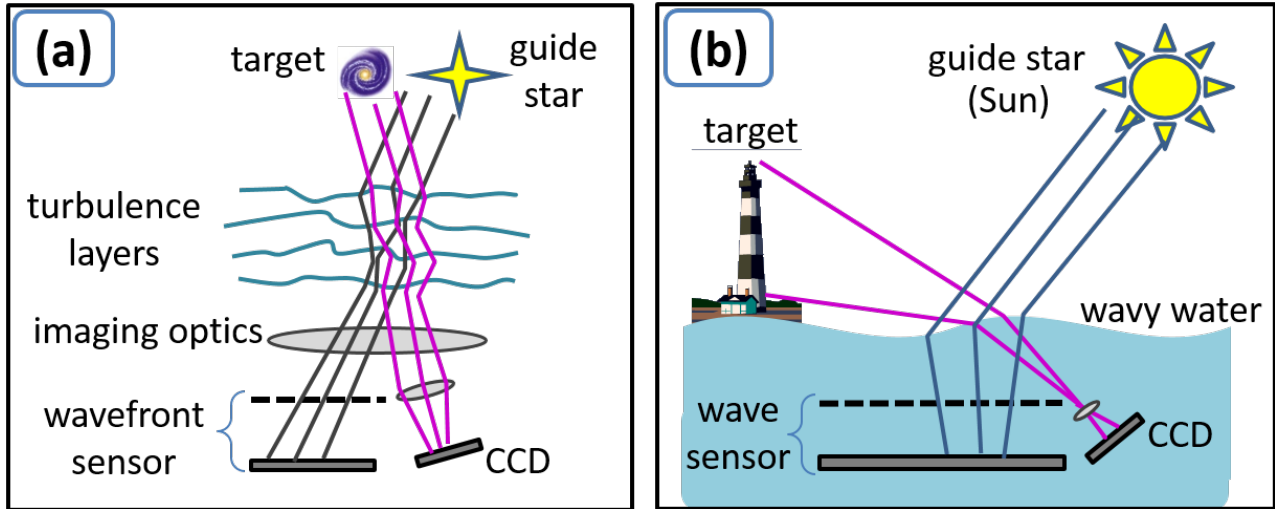


Figure 8. (a) Astronomy suffers from random refractive disturbances caused by atmospheric turbulence. The disturbance is estimated based on a wavefront-sensor that measures a projection of a *guide star*. (b) A submerged virtual periscope suffers from random refractive disturbances caused by a wavy water-air interface. The disturbance is estimated based on a surface-slope-sensor (wave sensor). Here the guide star is the *Sun*. In both cases, the disturbance estimate enables its partial compensation. © 2014 IEEE. Reprinted, with permission, from *Stella Maris: Stellar MARine Refractive Imaging Sensor* by Alterman et al, Proc. ICCP.

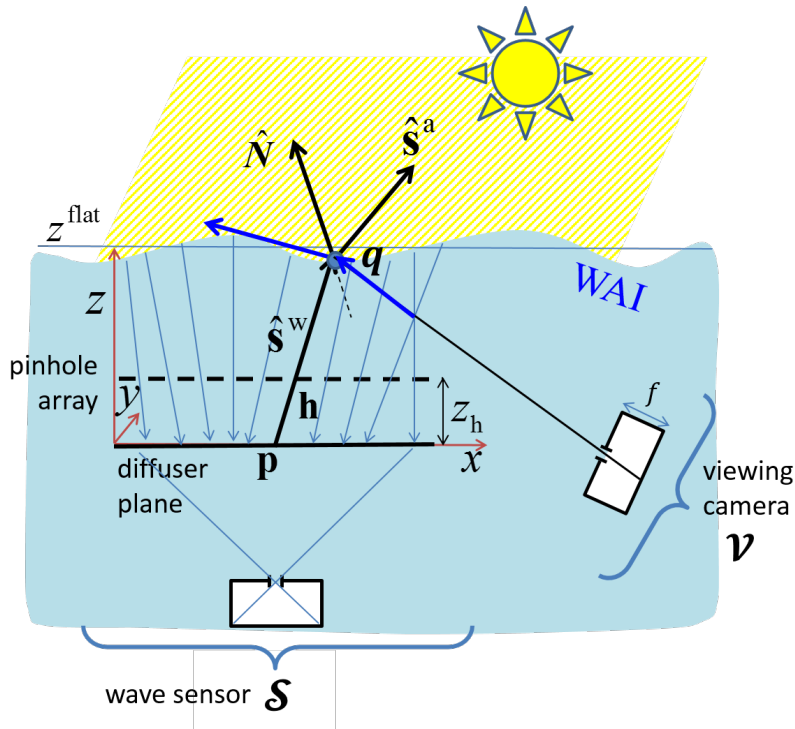


Figure 9. Geometry of a stellar marine refractive imaging sensor (STELLA MARIS), comprising a slope-sensor \mathcal{S} , a viewing camera \mathcal{V} , and the Sun pointed by airborne vector $\hat{\mathbf{s}}^a$.

The sample normal $\hat{\mathbf{N}}$ corresponds to 3D point \mathbf{q}_k . However, \mathbf{q}_k is unknown, since the WAI is unknown.

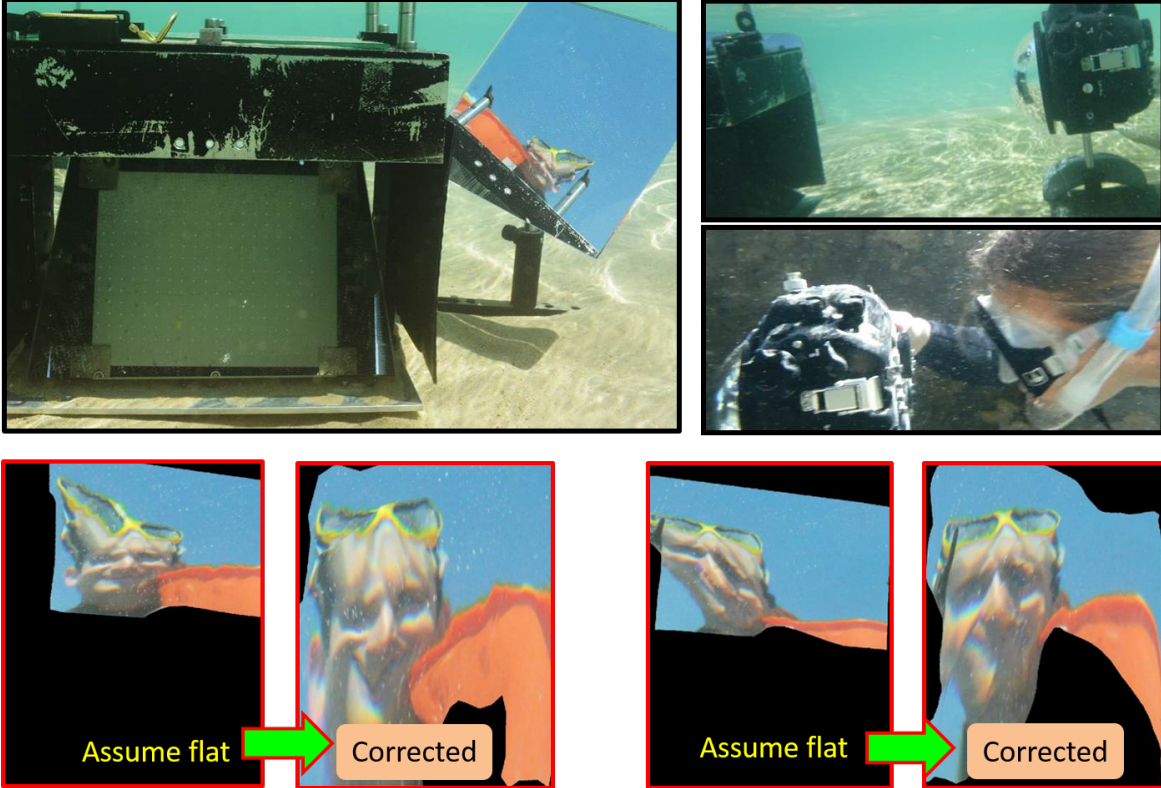


Figure 10. Oceanic experiment. [Top] Experimental setup. [Bottom] Analysis of two frames: flat-water assumption compared to our recovery. © 2014 IEEE. Reprinted, with permission, from *Stella Maris: Stellar MARine Refractive Imaging Sensor* by Alterman et al, Proc. ICCP.

Thus, we artificially set the WAI to be flat, at altitude z^{flat} above the diffuser plane. Then,

$$\mathbf{q}_k \approx (q_x, q_y, z^{\text{flat}}) = \mathbf{p}_k + \hat{\mathbf{v}}_w z^{\text{flat}} / s_z^w. \quad (14)$$

Surface estimation from its sampled normals $\{\hat{\mathbf{N}}_k\}$ is closely related to shape from shading.^{28,29} The WAI is typically smooth and integrable. Thus, we perform numerical integration of the WAI gradient field (slopes field), which is derived from $\{\hat{\mathbf{N}}_k\}$. We use the integration method of Ref.³⁰ to estimate the 3D WAI shape.

In our implementation, the pinhole array was a thin metal sheet manufactured using precise laser cutting. It was laid on a glass plate. The diffuser was made of opal glass. The camera was a Nikon D7100. System calibration is described in.³¹ System leveling was verified by a leveler. We had $D = 1.8\text{cm}$, $z_h = 6.18\text{cm}$ and $z^{\text{flat}} = 25.7\text{cm}$. Exposure time was 4ms. System azimuth was measured by a compass.

We made a sea test session, near Dado Beach (Haifa), illustrated in Fig. 10. Compensation assuming solely flat-water distortion is compared to recovery based on the wave sensor. Compensation relied on knowledge that a person was standing at horizontal distance of 75cm from the system. Additional experiments are detailed in our full length paper.²⁶ We experienced failure cases when the WAI experienced small scale wave ripples. Our existing implementation does not sample the WAI densely enough to measure such high frequency waves, yielding WAI aliasing.

5. DISCUSSION

This paper presented several approaches for imaging through natural random refractive media. We describe passive estimation of a volumetric spatially varying distribution of turbulence-strength. As the approach does

not require synchronization between cameras, it can be used with simple hardware deployed in a wide range of scales. More broadly, webcams observe cities worldwide, some over long ranges.³² Their locations and viewing directions³³ can be used with our framework for potentially large-scale turbulence measurements.

For triangulation through water, we used a stereo camera pair that acquired several temporal frames. The formulation is stochastic, and optimal estimation is obtained in the sense of maximum likelihood. Furthermore, the approach yields the location uncertainty, by the effective support of the 3D likelihood function. This approach may be generalized to detection and analysis of moving objects, through dynamic random refraction by acquiring many images simultaneously. The method could be used to image through atmospheric turbulence where distortions are typically less severe. However, the operating ranges are much longer.

Finally, we proposed deterministic correction for water distortion. The correction is assisted by light-field imaging of the Sun. This imaging passively measures the water waves. Then, the recovered water surface is used to compensate for distortions in a scene of interest, captured simultaneously. Distortions can be reduced but some distortions remain. Nevertheless, images corrected by the process can later be handled by statistical un-distortion post-processes,^{34–38} such as lucky imaging,^{39–41} stochastic triangulation,²⁴ and motion detection.⁴²

There are many ways to advance this concept. Using a lenslet array in the sensor instead of pinholes would increase efficiency. To break the correspondence constraint, it is possible to color-encode pinholes/lenslets.^{16,43} The sensor can be tilted towards the obliquely-illuminating Sun with the help of orientation sensors, instead of a leveler.

6. ACKNOWLEDGMENTS

This research was conducted in the Ollendor Minerva Center. Minerva is funded through the BMBF. We thank Yohay Swirski, Srinivasa Narasimhan, Minh Vo for the collaboration; Joseph Shamir for useful discussions; Johanan Erez, Ina Talmon and Dani Yagodin for technical support; and Vadim Holodovsky, Tali Treibitz, Danny Veikherman, Amit Aides, Aviad Levis, Yahel David, Guy Nir, Roy Or-El and Mark Sheinin for helping with the experiments. We thank the swimming pool facilities of the Technion and Zohar Bakfar B & B for enabling experiments in their swimming pool. Yoav Schechner is a Landau Fellow - supported by the Taub Foundation. The work in the Technion group is supported by the Israel Science Foundation (ISF Grant 1467/12), the R. L. Kohns Eye Research Fund and the Asher Space Research Fund. Marina Alterman was funded in part by ONR Grant #N00014-15-1-2735.

REFERENCES

- [1] Ihrke, I., Kutulakos, K., Lensch, H. P., Magnor, M. A., and Heidrich, W., “State of the art in transparent and specular object reconstruction,” in [*Proc. Eurographics*], (2008).
- [2] Miyazaki, D. and Ikeuchi, K., “Shape estimation of transparent objects by using inverse polarization ray tracing,” *IEEE TPAMI*, 2018–2030 (2007).
- [3] Shan, Q., Curless, B., and Kohno, T., “Seeing through obscure glass,” *ECCV* (2010).
- [4] Tian, Y., Narasimhan, S., and Vannevel, A., “Depth from optical turbulence,” in [*Proc. IEEE CVPR*], (2012).
- [5] Kolmogorov, A. N., “Dissipation of energy in locally isotropic turbulence,” in [*Dokl. Akad. Nauk SSSR*], **32(1)**:, 16–18 (1941).
- [6] Kolmogorov, A. N., “The local structure of turbulence in incompressible viscous fluid for very large Reynolds numbers,” in [*Dokl. Akad. Nauk SSSR*], **30(4)**:, 299–303 (1941).
- [7] Oberlack, M., Peinke, J., Talamelli, A., Castillo, L., and Hölling, M., “Progress in Turbulence Wind Energy IV,” in [*Proc. iTi Conf. in Turbulence*], (2010).
- [8] Aides, A., Schechner, Y., Holodovsky, V., Garay, M., and Davis, A., “Multi sky-view 3D aerosol distribution recovery,” *Optics Express* **21(22)**, 25820–25833 (2013).
- [9] Atcheson, B., Ihrke, I., Heidrich, W., Tevs, A., Bradley, D., Magnor, M., and Seidel, H., “Time-resolved 3D capture of non-stationary gas flows,” *ACM TOG* **27(5)**, 132:1–132:9 (2008).
- [10] Yamashita, K., Yendo, T., Tehrani, M. P., Fujii, T., and Tanimoto, M., “High-efficiency acquisition of ray-space using radon transform,” *Proc. SPIE* **7690**, 76900K–76900K–9 (2010).

- [11] Hargather, M. and Settles, G., “Natural-background-oriented schlieren imaging,” *Experiments in fluids* **48**(1), 59–68 (2010).
- [12] Ma, C., Lin, X., Suo, J., Dai, Q., and Wetzstein, G., “Transparent object reconstruction via coded transport of intensity,” in [*Proc. IEEE CVPR*], (2014).
- [13] Messer, H., Zinevich, A., and Alpert, P., “Environmental sensor networks using existing wireless communication systems for rainfall and wind velocity measurements,” *IEEE Instrum. Meas. Mag.*, 32–38 (2012).
- [14] Schechner, Y., Diner, D., and Martonchik, J., “Spaceborne underwater imaging,” in [*Proc. IEEE ICCP*], (2011).
- [15] Trifonov, B., Bradley, D., and Heidrich, W., “Tomographic reconstruction of transparent objects,” in [*Proc. Eurographics Symposium on Rendering*], 51–60 (2006).
- [16] Wetzstein, G., Roodnick, D., Raskar, R., and Heidrich, W., “Refractive shape from light field distortion,” in [*Proc. IEEE ICCV*], (2011).
- [17] Bitman, A., Goldring, S., Moshe, I., and Zalevsky, Z., “Computed tomography using broadband bessel thz beams and phase contrast,” *Opt. Lett.* **39**(7), 1925–1928 (2014).
- [18] Alterman, M., Schechner, Y. Y., Vo, M., and Narasimhan, S. G., “Passive tomography of turbulence strength,” in [*Proc. ECCV 2014*], 47–60, Springer (2014).
- [19] Kopeika, N. S., [*A System Engineering Approach to Imaging*], SPIE Press (1998).
- [20] Hansen, P. C. and Saxild-Hansen, M., “AIR tools MATLAB package of algebraic iterative reconstruction methods,” *J. Computational and Applied Mathematics* **236**(8), 2167 – 2178 (2012).
- [21] Zamek, S. and Yitzhaky, Y., “Turbulence strength estimation from an arbitrary set of atmospherically degraded images,” *JOSA A* **23**(12), 3106–3113 (2006).
- [22] Schechner, Y. Y., “Stereo from flickering caustics data and results.” [Online]. Available: http://webee.technion.ac.il/~yoav/research/turbulence_tomography.html.
- [23] Son, J.-Y. and Javidi, B., “Three-dimensional imaging methods based on multiview images,” *J. Display Technol.* **1**(1), 125 (2005).
- [24] Alterman, M., Schechner, Y., and Swirski, Y., “Triangulation in random refractive distortions,” in [*Proc. IEEE ICCP*], (2013).
- [25] Xiao, X., Javidi, B., Martinez-Corral, M., and Stern, A., “Advances in three-dimensional integral imaging: sensing, display, and applications,” *Appl. Opt.* **52**, 546–560 (Feb 2013).
- [26] Alterman, M., Swirski, Y., and Schechner, Y., “STELLA MARIS: Stellar marine refractive imaging sensor,” in [*Proc. IEEE ICCP*], (2014).
- [27] Kidger, M. J., [*Fundamental Optical Design*], SPIE Press (2002).
- [28] Narasimhan, S., Nayar, S., Sun, B., and Koppal, S., “Structured light in scattering media,” in [*IEEE ICCV*], **1**, 420–427 (2005).
- [29] Sato, I., Okabe, T., and Sato, Y., “Bispectral photometric stereo based on fluorescence,” in [*IEEE CVPR*], 270–277 (2012).
- [30] Moisy, F., Rabaud, M., and Salsac, K., “A synthetic Schlieren method for the measurement of the topography of a liquid interface,” *Exper. in fluids* **46**(6), 1021–1036 (2009).
- [31] Authors, “Supplemental material - calibration,”
- [32] Lalonde, J., Efros, A., and Narasimhan, S., “Webcam clip art: Appearance and illuminant transfer from time-lapse sequences,” *ACM TOG* **28**(5), 131:1–131:10 (2009).
- [33] Lalonde, J., Narasimhan, S., and Efros, A., “What do the sun and the sky tell us about the camera?,” *IJCV* **88**(1), 24–51 (2010).
- [34] Murase, H., “Surface shape reconstruction of a nonrigid transport object using refraction and motion,” *IEEE TPAMI* **14**, 1045–1052 (1992).
- [35] Oreifej, O., Shu, G., Pace, T., and Shah, M., “A two-stage reconstruction approach for seeing through water,” in [*Proc. IEEE CVPR*], (2011).
- [36] Tian, Y. and Narasimhan, S. G., “Seeing through water: Image restoration using model-based tracking,” in [*Proc. IEEE ICCV*], 2303–2310 (2009).
- [37] Tian, Y. and Narasimhan, S. G., “A globally optimal data-driven approach for image distortion estimation,” in [*Proc. IEEE CVPR*], (2010).

- [38] Wen, Z., Lambert, A., Fraser, D., and Li, H., “Bispectral analysis and recovery of images distorted by a moving water surface,” in [*JOSA A*], **49:33**, 6376–6384 (2010).
- [39] Donate, A. and Ribeiro, E., “Improved reconstruction of images distorted by water waves,” *ICCV*, 228–235 (2006).
- [40] Efros, A., Isler, V., Shi, J., and Visontai, M., “Seeing through water,” *NIPS* **17**, 393–400 (2004).
- [41] Suiter, H., Flacco, N., Carter, P., Tong, K., Ries, R., and Gershenson, M., “Optics Near the Snell Angle in a Water-to-Air Change of Medium,” in [*Proc. IEEE OCEANS*], (2008).
- [42] Alterman, M., Schechner, Y. Y., Shamir, J., and Perona, P., “Detecting motion through dynamic refraction,” *IEEE TPAMI* **35**, 245–251 (2013).
- [43] Zhang, X. and Cox, C. S., “Measuring the two-dimensional structure of a wavy water surface optically: A surface gradient detector,” *Exper. in Fluids* **17**, 225–237 (1994).